



Observation of a Large Lee Wave in the Drake Passage

JESSE M. CUSACK AND ALBERTO C. NAVEIRA GARABATO

University of Southampton, and National Oceanography Centre, Southampton, United Kingdom

DAVID A. SMEED

National Oceanography Centre, Southampton, United Kingdom

JAMES B. GIRTON

Applied Physics Laboratory, University of Washington, Seattle, Washington

(Manuscript received 28 June 2016, in final form 23 January 2017)

ABSTRACT

Lee waves are thought to play a prominent role in Southern Ocean dynamics, facilitating a transfer of energy from the jets of the Antarctic Circumpolar Current to microscale, turbulent motions important in water mass transformations. Two EM-APEX profiling floats deployed in the Drake Passage during the Diapycnal and Isopycnal Mixing Experiment (DIMES) independently measured a 120 ± 20 -m vertical amplitude lee wave over the Shackleton Fracture Zone. A model for steady EM-APEX motion is developed to calculate absolute vertical water velocity, augmenting the horizontal velocity measurements made by the floats. The wave exhibits fluctuations in all three velocity components of over 15 cm s^{-1} and an intrinsic frequency close to the local buoyancy frequency. The wave is observed to transport energy and horizontal momentum vertically at respective peak rates of $1.3 \pm 0.2 \text{ W m}^{-2}$ and $8 \pm 1 \text{ N m}^{-2}$. The rate of turbulent kinetic energy dissipation is estimated using both Thorpe scales and a method that isolates high-frequency vertical kinetic energy and is found to be enhanced within the wave to values of order $10^{-7} \text{ W kg}^{-1}$. The observed vertical flux of energy is significantly larger than expected from idealized numerical simulations and also larger than observed depth-integrated dissipation rates. These results provide the first unambiguous observation of a lee wave in the Southern Ocean with simultaneous measurements of its energetics and dynamics.

1. Introduction

Lee waves can be generally defined as internal gravity waves generated by the interaction of a quasi-steady stratified flow with topography. Observations of such phenomena in the ocean are rare, with notable examples including high-frequency, tidally forced waves in the lee of ridges (e.g., Pinkel et al. 2012; Alford et al. 2014). Propagating waves must have a frequency between the local inertial frequency f and buoyancy frequency N ,

which precludes their generation in many regions of the ocean where bottom flows are not sufficiently strong and topography is not of the correct scale to excite such a frequency. Global maps of energy input to lee waves from geostrophic flows (Scott et al. 2011; Nikurashin and Ferrari 2011) highlight the importance of the Southern Ocean because it contains many regions that meet the dynamical requirements, usually centered on ridges and fracture zones such as Phoenix Ridge and the Shackleton Fracture Zone (SFZ) in Drake Passage. Lee waves extract energy and horizontal momentum from the forcing flow and can transport them both vertically and

Denotes content that is immediately available upon publication as open access.

Corresponding author e-mail: Jesse Cusack, jesse.cusack@noc.soton.ac.uk



This article is licensed under a Creative Commons Attribution 4.0 license (<http://creativecommons.org/licenses/by/4.0/>).

horizontally, redistributing them throughout the water column via nonlinear interactions with other waves, the large-scale flow, or instabilities that result in wave breaking (e.g., Munk 1980). Lee waves have garnered growing interest in recent years, as efforts have been made to understand the origins of small-scale turbulence and its role in returning dense waters to the upper layers of the ocean as part of the global overturning circulation (Talley 2013; Waterhouse et al. 2014).

Turbulent kinetic energy dissipation (TKED) and mixing are consistently found to be enhanced over regions of rough bathymetry, using a variety of measurement techniques including tracer releases and microstructure profiles (Ledwell et al. 2000; Watson et al. 2013). The presence of lee waves in these regions is usually inferred from finescale (order 100 m) measurements of variance in velocity shear and isopycnal strain, which show a predominance of upward-traveling wave energy (Naveira Garabato et al. 2004; Kunze et al. 2006; Waterman et al. 2013; Sheen et al. 2013) indicative of bottom generation. In addition, a more limited number of microstructure profiles indicates that turbulent kinetic energy dissipation is enhanced within \sim 1 km of the ocean floor over topography (St. Laurent et al. 2012; Sheen et al. 2013). Shear- and strain-based parameterization methods (e.g., Polzin et al. 2014) are also used to estimate dissipation rates, and while there is currently an unresolved quantitative discrepancy between these results and those from microstructure (Hibiya et al. 2012; Waterman et al. 2014), the qualitative picture of bottom-enhanced dissipation is robust. The inference from this range of observations is that lee waves are generated over rough bathymetry and eventually break, causing turbulence in the vicinity of the topography. However, this picture remains open to alternative interpretations, as the unambiguous observation of lee waves in the Southern Ocean has remained elusive.

It has been appreciated in the atmospheric literature that lee waves, or mountain waves, play an important role in the momentum budget and influence aspects of the general circulation (e.g., Fritts 2003) and that the results of general circulation models are improved when their effects are accounted for (McFarlane 1987). The dominant momentum balance in the Antarctic Circumpolar Current (ACC) is between wind stress at the surface and form stress across large bathymetric features, such as ridges, on scales of 1000 km (Vallis 2006). Further, recent work estimating the lee-wave drag on the geostrophic flow from an application of wave radiation theory suggests that regions of the ACC with rough bathymetry of the required lateral scale to excite waves (1–10 km) may add a nonnegligible wave drag to the momentum balance (Naveira Garabato et al. 2013).

Direct measurements of lee-wave momentum fluxes and convergence in the Southern Ocean are required to test this hypothesis. The results would have implications for numerical models that do not resolve small-scale topography and internal waves, since their effect on the momentum balance would need to be parameterized.

In this paper, we document the first observations of a lee wave in the Southern Ocean and determine its properties, fluxes of energy and horizontal momentum and turbulent kinetic energy dissipation levels. The observations were obtained with two electromagnetic autonomous profiling explorer (EM-APEX) floats deployed in Drake Passage under the auspices of the Diapycnal and Isopycnal Mixing Experiment in the Southern Ocean (DIMES), a U.S.–U.K. program to investigate mixing processes in the ACC (Gille et al. 2007). Previous investigations of internal waves using EM-APEX floats have focused on diagnosing near-inertial waves, which oscillate with a time period of approximately 14 h at 57°S, significantly longer than the time it takes to profile (Kilbourne and Girton 2015; Meyer et al. 2016). Here, we focus on the measurement of a near-buoyancy frequency wave with a period close to 1 h in a frame of reference moving with the mean flow. This has presented new challenges in analysis because time dependence cannot be neglected. Several methods for estimating vertical water velocity and turbulent kinetic energy dissipation are adapted and applied to the measurements, allowing almost complete characterization of the wave in terms of frequency, wavelength, momentum flux, energy flux, and dissipation rate.

A description of the floats and data sampling strategy is provided in section 2, which also includes an assessment of a theoretical model of profiling float motion used to calculate absolute vertical water velocity. In section 3, the float measurements are used to characterize the observed lee wave and estimate its associated fluxes of energy and momentum and turbulent dissipation rates. A discussion of the significance of our findings for the emerging picture of the role of lee waves in the Southern Ocean circulation is offered in section 4, followed by concluding remarks.

2. Data and methods

a. Instrumentation and sampling strategy

The primary observations of this work were obtained by two EM-APEX floats, numbered 4976 and 4977, deployed at the same time and position in the Drake Passage from the Royal Research Ship (RRS) *James Cook* (57°34'14.9"S, 68°11'1.4"W) on 31 December 2010 at 1218 UTC. Float trajectories are displayed in Fig. 1. EM-APEX floats, described in greater detail by Sanford et al. (2005), are modified APEX floats that were

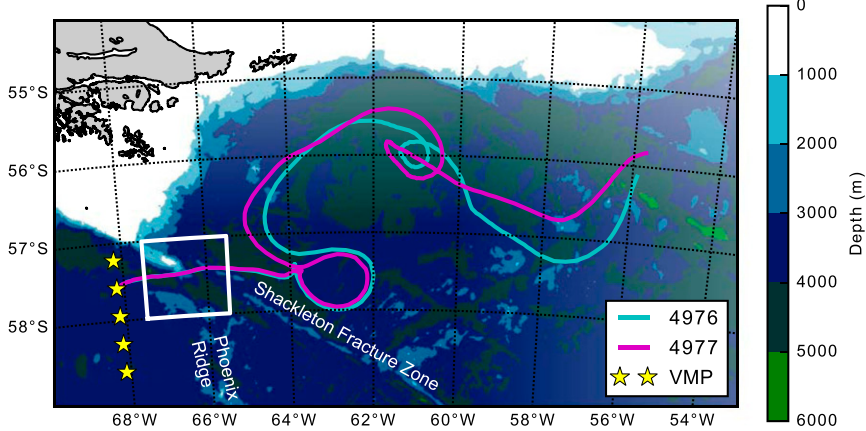


FIG. 1. Map of the northern Scotia Sea with float trajectories and vertical microstructure profiler stations (VMP) used in calibrating the float-derived dissipation rates. Lee-wave measurements were obtained within the boxed region, which is expanded in Fig. 6.

developed at the Applied Physics Laboratory, University of Washington, in collaboration with Teledyne Webb Research Corporation. Electrodes on the outer casing measure the potential difference across the instrument induced by the motion of the ocean through the vertical component of Earth's magnetic field (Sanford 1971). This information, along with measurements of instrument tilt and magnetic compass heading, is used to calculate relative horizontal water velocity with a characteristic precision of 1 cm s^{-1} . Relative velocity is converted to absolute velocity by using surface GPS positions to estimate a depth-independent constant offset. The floats are also equipped with a Seabird Electronics SBE-41 pumped CTD.

Using a piston to pump oil into and out of an external bladder, the floats were programmed to change their buoyancy in such a way as to maintain an approximately constant vertical speed of 12 cm s^{-1} . The position of the piston was recorded and transmitted along with measurements from the EM system, CTD, and GPS position via Iridium telecommunication satellites while at the surface. The sampling frequency varied but on average CTD measurements were made every 20 s or 2.5 m, while EM measurements were made every 25 s or 3 m. Both floats analyzed here were programmed to profile continuously to 1500 dbar, taking about 3.5 h to complete an ascent or descent, pausing only while at the surface for an average of 30 min to transmit data.

b. Derived variables

Analysis was performed on several variables not directly observed by the floats, and their derivation is described here briefly. Relative horizontal velocity measurements were converted to absolute horizontal velocity using the

method described by Phillips and Bindoff (2014). In summary, the relative horizontal velocity measured from a descent/ascent profile pair is integrated with respect to time, providing a displacement estimate. The difference between this displacement and the measured GPS displacement at the surface is then divided by the time taken to profile and constitutes a constant depth-independent velocity that is added back to the relative velocity. This method also provides an estimate for subsurface float position (x, y), in meters, in the zonal and meridional direction from the point of descent.

In situ and potential density as well as buoyancy frequency were calculated from CTD temperature, salinity, and pressure measurements using the International Thermodynamic Equation Of Seawater—2010 (TEOS-10; IOC et al. 2010). Smooth reference potential density profiles referenced to 1000 dbar ρ_{ref} were computed by averaging five profiles before and after the target profile. Density perturbations ρ' were calculated by subtracting reference density from measured density. Smooth “reference” buoyancy frequency profiles were generated using the adiabatic levelling method (Bray and Fofonoff 1981; Millard et al. 1990). Pressure perturbation was estimated by integrating buoyancy perturbation, $b' = -gp'/\rho_0$, where ρ_0 is the mean density, with depth, assuming hydrostatic balance before subtracting the depth average, using a method described by Kunze et al. (2002) and further analyzed by Nash et al. (2005).

c. Estimation of vertical velocity

1) DERIVATION

Following previous work on the estimation of oceanic vertical flow from gliders (Merckelbach et al. 2010; Frajka-Williams et al. 2011), we have developed a

theoretical model describing the vertical motion of EM-APEX floats in a stratified, stationary fluid. After optimization of the model parameters, absolute vertical water velocity w is estimated as the difference between the measured float vertical velocity w_m and the steady vertical velocity that it is predicted to have in still water w_s :

$$w = w_m - w_s, \quad (1)$$

where $w_n = dz_m/dt$. Float height z_m is determined from pressure and latitude using the TEOS-10 package. To determine w_s , it is necessary to solve the steady equation of motion of the float:

$$M \frac{dw_s}{dt} = g(M - \rho V) - \rho C_D A |w_s| w_s, \quad (2)$$

with

$$\frac{dz_s}{dt} = w_s, \quad (3)$$

where z_s is the float height in still water, the first term on the right of Eq. (2) is the buoyancy force, and the second term is a quadratic drag force suitable for an object fully immersed in a high Reynolds number flow (Batchelor 2000). The variables are gravitational acceleration g , float mass M , water density ρ , float volume V , float cross-sectional area A , and a nondimensional drag coefficient C_D . The float volume is a function of pressure and the volume of oil pumped into the external bladder. In principle, it is necessary to solve the system of differential equations described by Eqs. (2) and (3) to fully determine w_s . However, if a steady force balance is assumed, setting $dw_s/dt = 0$, the equations can be simplified.

Given a steady-state assumption, Eq. (2) can be rearranged for w_s as

$$w_s = \text{sign}(\rho V - M) \sqrt{\frac{|g(M - \rho V)|}{\rho C_D A}}. \quad (4)$$

Float volume is assumed to change linearly with pressure p and piston position k :

$$V = V_0[1 + \alpha_p(p - p_0)] + \alpha_k(k - k_0), \quad (5)$$

where V_0 , p_0 , and k_0 denote the volume, pressure, and piston position at the ballast point. Variables α_p and α_k are the coefficient of compressibility and the change in volume with piston position, respectively. We have neglected the effects of thermal expansion because they are difficult to separate from those of pressure, since in this area of the ocean both sets of effects cause a

decrease in volume with depth. Variations in temperature during profiles do not typically exceed 5°C , and if a thermal expansion coefficient of $3.6 \times 10^{-5}^\circ\text{C}^{-1}$ (as quoted in the technical specifications for EM-APEX floats) is assumed, then thermal changes in volume over a profile are typically one order of magnitude smaller than compressive changes and thus can justifiably be neglected.

2) OPTIMIZATION

The steady model contains seven parameters, of which mass, ballast piston position, and ballast pressure are known, having been measured or set prior to deployment. The float diameter is 16.5 cm, giving a cross-sectional area of 0.02 m^2 that is assumed to remain constant with depth. In subsequent calculations the area is combined with the drag coefficient into a single parameter C_D^* , the value of which is not initially known. The remaining parameters are optimized by minimizing the following cost function for vertical water velocity variance over many profiles:

$$\sum_t w(t)^2, \quad (6)$$

where $w(t)$ denotes any absolute water velocity measurement at time t regardless of depth. This cost function follows from conservation of volume in an incompressible fluid, which is a very good approximation for the entire ocean but is also assumed to hold over the smaller spatial and time scales covered by a float. We defer to Frajka-Williams et al. (2011) for a more thorough discussion of cost functions. In summary, they assessed four, including Eq. (6), and found that one was as effective as Eq. (6), while two were worse and did not produce physically consistent results.

Standard least squares methods were used to perform the optimization separately for each float, using 150 profiles shortly after the lee wave was observed. Parameter estimates from technical specifications were used as initial values. It is possible that parameter values may change over the lifetime of a float, for example, the drag coefficient can change as a result of biofouling (Merckelbach et al. 2010). Profiles to optimize were chosen so that the model would be reliable at the time of the lee-wave observation, while also keeping the observations independent from the model parameters. The resulting parameters and their uncertainties are summarized in Table 1, along with values expected from technical specifications. Uncertainties were estimated by repeating the optimization many times on random subsamples of the chosen profiles to build a distribution of possible parameters from which the standard deviation was calculated. Over a small range of parameter

TABLE 1. Vertical velocity model parameter estimates after optimization for the two floats are displayed in the latter two columns, including the one standard deviation uncertainty. Expected values come from technical specifications for EM-APEX.

Parameter	Units	Expected	Float 4976	Float 4977
V_0	10^{-2} m^3	2.62	2.62 ± 0.0	2.62 ± 0.0
C_D^*	10^{-2} m^2	2.9	3.5 ± 0.6	2.2 ± 0.4
α_p	$10^{-6} \text{ dbar}^{-1}$	3.67	3.6 ± 0.3	3.8 ± 0.2
α_k	10^{-6} m^3	1.156	1.5 ± 0.3	1.0 ± 0.2

values close to the optimum, C_D^* and α_k covary with compensating effect on vertical velocity. This may have resulted in a somewhat unrealistic, albeit small, difference between these parameters for the two floats.

3) VALIDATION AND UNCERTAINTIES

Without independent measurements of vertical velocity with which to compare, only a limited validation of the model is possible. The first check is the distribution of vertical velocities, which should be centered on zero, as constrained by the optimization procedure. Figure 2 shows the distribution of measurements. This closely approximates a Gaussian distribution with a mean of 0.0 mm s^{-1} and a standard deviation of 9 mm s^{-1} . In total, 51% of velocities are less than 1 cm s^{-1} .

The Garrett–Munk (GM) spectrum (e.g., Gregg and Kunze 1991) provides an estimate of the expected internal wave–induced variance of several physical quantities, including vertical velocity or vertical kinetic energy (VKE; Thurnherr et al. 2015) as a function of vertical wavenumber:

$$\text{VKE}(m) = \pi E_0 b N f j_* \frac{1}{(m + m_*)^2}, \quad (7)$$

where the nondimensional spectral energy level $E_0 = 6.3 \times 10^{-5}$; b is the stratification e -folding scale taken as 1000 m in the Drake Passage (Thurnherr et al. 2015); j_* is the peak wavenumber, which quantifies the bandwidth of the internal wave field; $m_* = j_*(\pi N)/(bN_0)$; and $N_0 = 5.3 \times 10^3 \text{ rad s}^{-1}$.

Analysis of vertical velocity from lowered acoustic Doppler current profilers (LADCPs) measurements (Thurnherr et al. 2015) find that such a spectrum holds in many regions of the ocean, spanning a range of latitudes, up to a limiting wavenumber. The average VKE spectrum from the two floats, computed from 100 profiles distant from the observed wave, is compared to the GM spectrum in Fig. 3. In general, the GM spectrum with default parameter values is about a factor of 2 more energetic than the measured average spectrum but is still encompassed by the spread of individual profile spectra, denoted in the figure by faint

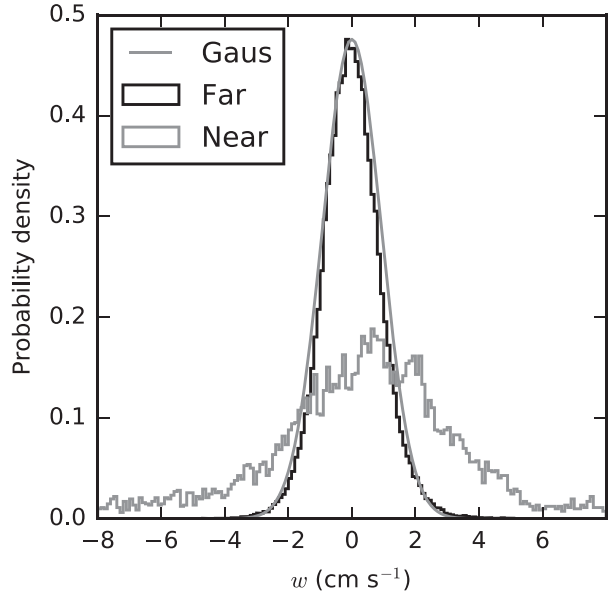


FIG. 2. Histogram of vertical velocity measurements from depths greater than 50 m. The results from both floats have been combined. The black histogram contains observations from the far field that were used to optimize the velocity model. The gray histogram contains observations from the area of the wave observation, the same profiles displayed in Fig. 4. A Gaussian with zero mean and 0.9 cm s^{-1} standard deviation is shown for reference.

gray lines. Measured energy levels decline from large to small vertical scales at a rate that is consistent with the power law proportional to m^{-2} over the wavenumber range 0.03 to 0.2 rad m^{-1} . A notable deviation from this power law includes a broad peak at 0.02 rad m^{-1} . This is likely caused by processes with a time scale of $2\pi/N$ aliasing the spatial signal, since for a float traveling at $w_f \approx 0.12 \text{ m s}^{-1}$, and $N \approx 2 \times 10^{-3} \text{ rad s}^{-1}$, $N/w_f \approx 0.02 \text{ rad m}^{-1}$.

The standard deviation in vertical velocity from different choices in model parameter, estimated from the distributions generated when optimizing the model, is 1 mm s^{-1} . This is an uncertainty that manifests as a constant bias in the profile velocity. An additional uncertainty of 1 mm s^{-1} at high frequencies is caused by random noise from the pressure sensor. The final source of uncertainty is introduced by a systematic bias in the model as a result of necessary simplification of float dynamics. A test on the accuracy of the steady model was performed by solving the fully time-dependent equations of motion and comparing to the time-independent solution (not shown). The difference between solutions was found to be greatest where the float was undergoing acceleration, such as at the beginning and end of profiles, and when the piston was moved to alter buoyancy. Synthetic profiles of

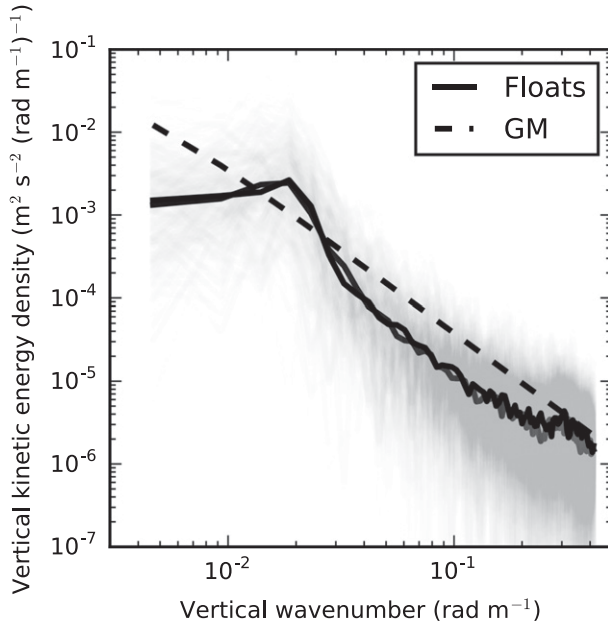


FIG. 3. Vertical kinetic energy spectrum from 100 profiles each from both floats (faint gray shading) as well as the mean (solid black) plotted against vertical wavenumber. The peak at 0.02 rad m^{-1} is likely caused by aliasing. The reference GM spectrum is also shown (dashed black).

density and pressure were generated, and the time response of the equations to a step change in piston position was assessed. It was found that the float reached 99% of the new terminal velocity after 15 s, corresponding to a vertical distance of less than 1.5 m, which is smaller than the characteristic sampling distance. Thus, for measurements of processes changing on time scales longer than this adjustment time or over larger vertical distances, the no acceleration assumption is justifiable.

d. Estimation of internal wave properties

Internal wave properties are estimated by application of linear internal wave theory, summarized in the [appendix](#), to the measurements. Properties that can be deduced without knowledge of the wavenumber components are aspect ratio α , intrinsic frequency ω_0 , energy density E , and the vertical fluxes of energy and horizontal momentum, denoted $\overline{w'p'}$ and $(\overline{w'u'}, \overline{w'v'})$, respectively. To estimate the wave perturbation of horizontal velocity (u', v') , a linear background shear is removed from absolute horizontal velocity measurements.

To estimate the aspect ratio and intrinsic frequency, 14 sets of coherent velocity and buoyancy maxima/minima were identified from profiles using a peak detection algorithm and confirmed by eye. The amplitudes at the maxima/minima were then applied in Eqs. (A10) and (A11). By isolating maxima in this way we assume

that the variability is dominated by a single monochromatic wave. Energy density was calculated by isolating segments of velocity and buoyancy profiles that contained an integer number of wave oscillations, identified from subsequent maxima by eye, before computing the time average over those isolated sections following Eq. (A12). The sections used are those depicted in [Fig. 4](#). The vertical fluxes of energy and horizontal momentum were also estimated for the isolated segments following the same approach. The above quantities, deduced without attempting to estimate any wavenumber components, are referred to as the “observed” quantities.

The impact of background oceanographic variability (which is significantly larger in magnitude than instrumental noise) on the energy and momentum flux diagnostics was investigated by repeating the calculation with the addition of red noise with spectral properties, such as slope and energy level, given by a background spectrum. The background spectrum was computed by averaging the absolute velocity spectra from 100 profiles in the far field. The standard deviation of results after many repetitions is the error, quoted in subsequent analysis. Ultimately, the results are found to be insensitive to choices of the type and energy level of background variability used.

To deduce the wavenumber, we fit monochromatic plane waves to observations of velocity, buoyancy, and pressure perturbation. Once deduced, the wavenumber implies, following linear theory, values for all the quantities discussed above. The quantities deduced from this fitting are referred to as “plane wave” estimates. Two illustrative profiles are presented in [section 3](#). The fits take into account the combination of spatial and temporal variability present in the observations by using the depth measurement from the float’s pressure sensor, the horizontal position estimated from time-integrated horizontal velocity, and time from the internal clock. In this way, it was possible to account for advection of the float by the local flow field.

The fitting procedure optimizes five parameters: the three wavenumber components, the pressure perturbation amplitude induced by the wave, and an arbitrary phase shift. Doppler shifting was accounted for by using the mean horizontal velocity of each profile, and a background shear was subtracted from the horizontal velocity. Markov chain Monte Carlo methods were used to conduct the fitting and produce likelihood distributions for the parameter values. Likelihood distributions are proportional to the posterior probability distribution, which describes the probability that the model fits the data with given parameter values. The most likely parameter set is the best estimate of the parameter value and the width of

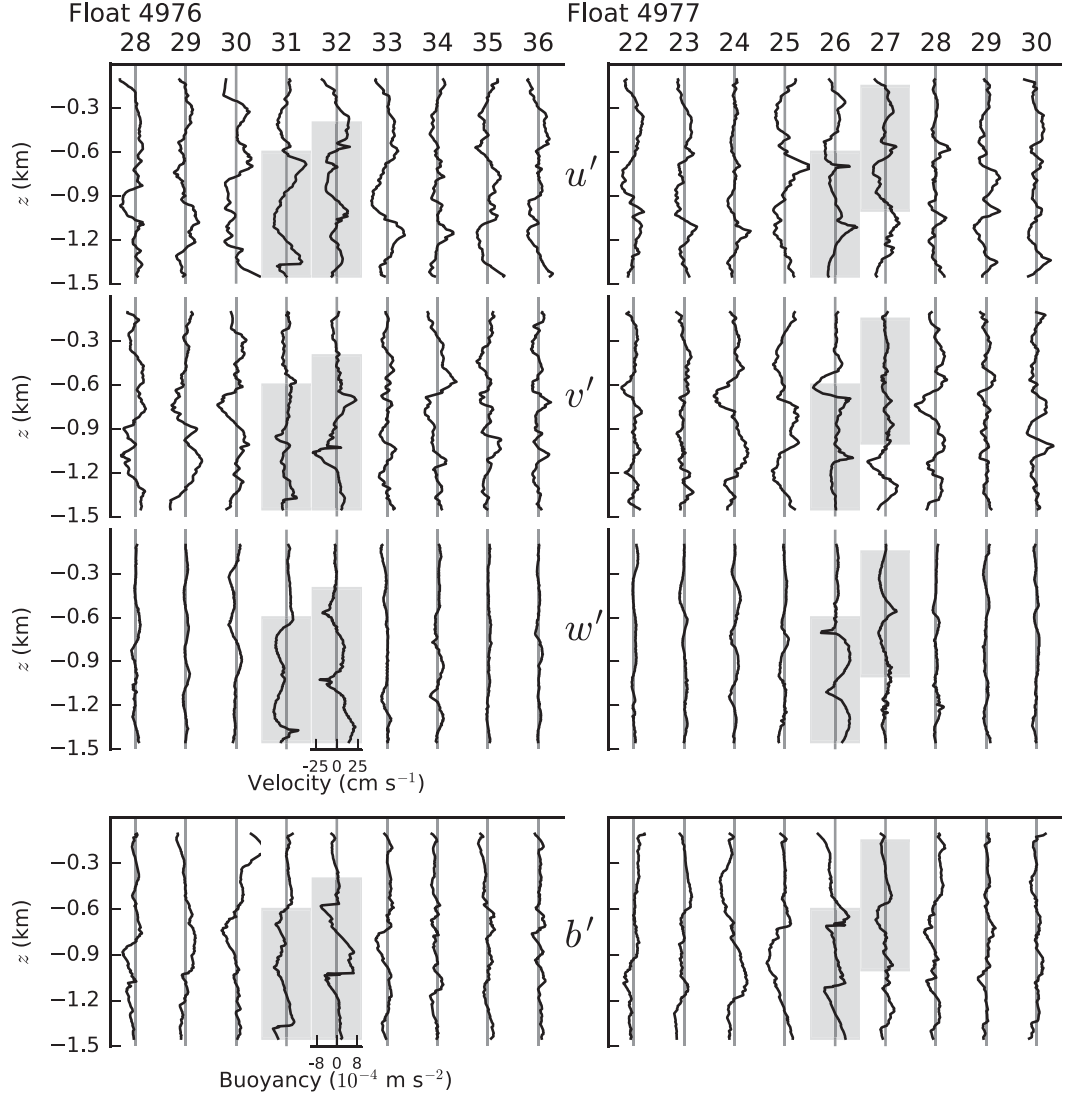


FIG. 4. An observed series of profiles for the two floats, split into rows of zonal u' , meridional v' , vertical velocity w' , and buoyancy b' . The observations are centered around the ridge crest and approximately correspond to the section of Fig. 6b between 0 and 20 km downstream of the ridge. Each minor column represents the results from a single profile and is numbered by its profile ID. The two major columns separate results for the two floats. The shaded regions mark segments of profiles that contain a coherent wave signal in multiple velocity components as well as a vertical velocity amplitude in excess of 10 cm s^{-1} .

the distribution is a measure of the confidence interval of that parameter set.

e. Estimation of the turbulent kinetic energy dissipation rate

To estimate the rate of turbulent kinetic energy dissipation rate ε , we employ the large-eddy method of [Beaird et al. \(2012\)](#), which has previously been applied to vertical velocity measurements from gliders. We also use the more established Thorpe-scale method ([Thorpe 1977; Dillon 1982](#)) for comparison.

1) LARGE-EDDY METHOD

The large-eddy method (LEM) can be derived from simple scaling of turbulent motions, specifically, the turbulent kinetic energy relation ([Taylor 1935](#)):

$$\varepsilon \sim \frac{q'^3}{l}, \quad (8)$$

where q' is the turbulent velocity scale and l is a length scale associated with the largest overturning eddies. The choice of an appropriate length scale is subject to certain

arbitrariness (Kantha and Clayson 2000). However, if one chooses the buoyancy length, defined as the vertical displacement over which a water parcel will convert its kinetic energy to potential energy in a stratified fluid and given nonrigorously as $q'N^{-1}$, then one arrives at the following equation:

$$\varepsilon = c\langle q'^2 \rangle N, \quad (9)$$

where c is a constant of proportionality. A complementary interpretation is that turbulent eddies are dissipated over a time proportional to N^{-1} , known as the eddy turnover time. An assumption of the method is that the largest turbulent scales are isotropic and that it is sufficient to measure the kinetic energy of one (in this case, the vertical) velocity component, equal to the mean square velocity $\langle q'^2 \rangle$ to estimate the energy of an overturn. Tests of the scaling (Beard et al. 2012, and references therein) indicate that it is valid for a range of oceanic conditions, including weak dissipation regimes, down to $q' \sim 0.2 \text{ mm s}^{-1}$ (Peters et al. 1995).

The constant of proportionality also corrects implicitly for limitations of the float vertical velocity model and for measurements that may not fully isolate turbulent motions and include small-scale internal waves. The vertical microstructure profile measurements made shortly before deployment of the floats (Sheen et al. 2013), marked as stars in Fig. 1, provide the best available calibration data. The statistics of ε from the large-eddy method and microstructure match for $c = 0.146$ (float 4976) and $c = 0.123$ (float 4977).

To isolate the vertical eddy velocity signal, first a temporal low-pass filter was applied to vertical velocity profiles with a cutoff period of 100 s. This was necessary to remove signals associated with internal electronic noise with an approximate length scale of 9 m resulting from a suspected time-stamp recording error, exhibited by both floats. The narrow bandwidth of the noise allowed for its complete removal. A spatial high-pass filter was then applied with a cutoff wavelength of 40 m. Steady height $z_s = \int w_s dt$ rather than measured height z was used as the spatial variable so as to reduce aliasing caused by changes in float profiling speed and advection by vertical flows. Root-mean-square vertical velocity and mean buoyancy frequency were calculated in a sliding 20-m window. Comparison of vertical kinetic energy spectra between profiles with high and low average ε values (not shown) indicate that energy is most enhanced at scales less than 100 m. The filter cutoff length scale is chosen pragmatically to capture this variance.

The vertical kinetic energy content at scales less than 40 m is likely to be dominated by internal waves for all but the most turbulent conditions, and as noted by Beard et al. (2012), the lack of a separation of scales between turbulence and waves makes it impossible to remove the wave signal. This might be expected to cause an overestimation of the dissipation rate; however, since the method is calibrated against microstructure measurements, the coefficient c is proportionally smaller to account for wave energy. The fact that the method theoretically relies on measuring the eddy energy rather than the wave energy remains a cause of concern. Some reassurance can be taken from the documented, albeit poorly understood, relationship between wave vertical kinetic energy and dissipation found by Thurnherr et al. (2015) in a variety of regions, including the Drake Passage. Thurnherr et al. (2015) use their findings as the basis for a new parameterization of dissipation in terms of VKE alone, which appears to provide more accurate results than shear-strain-based parameterizations. This is relevant because it implies that internal wave VKE is strongly connected to dissipation. We accept that some readers may not be convinced by the large-eddy method and so we also estimate dissipation using the more established Thorpe-scale method.

2) THORPE-SCALE METHOD

The theoretical basis of the Thorpe-scale method is that in a stratified fluid with buoyancy frequency N , the dissipation rate is related to the largest isotropic turbulent scales, defined by the Ozmidov scale L_O :

$$\varepsilon = L_O^2 N^3. \quad (10)$$

At scales larger than the Ozmidov scale, stratification suppresses vertical motion and turbulent eddies become anisotropic. At smaller scales, there exists an inertial subrange where energy cascades to the dissipation scale. By comparing a profile of density with the same data monotonically sorted, such that it forms a stable profile, it is possible to estimate the vertical displacement of density parcels in overturning regions. The Thorpe scale L_T is defined as the root-mean-square displacement of data in an overturn and empirically related to the Ozmidov scale by the relation $L_O = (0.8 \pm 0.4)L_T$ (Dillon 1982).

The method is sensitive to spurious density measurements, especially in weakly stratified regions of the water column, which may occur because of salinity spiking. To counter this problem we use the intermediate profile method of Ferron et al. (1998) and reject overturns using an overturn ratio criteria (Gargett and Garner 2008).

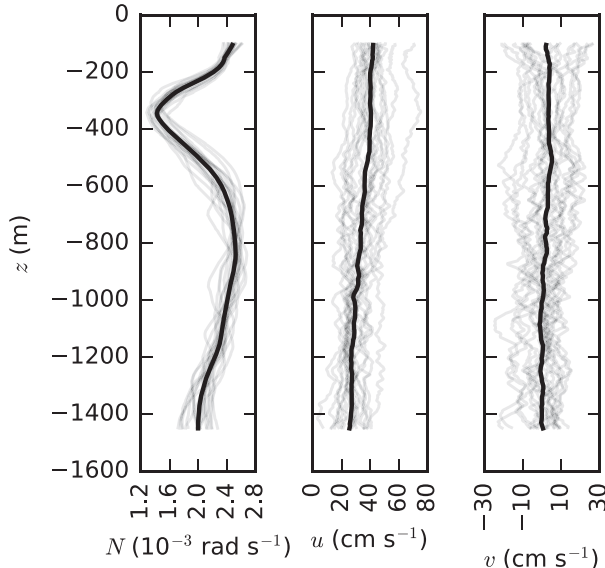


FIG. 5. Profiles (light gray) of buoyancy frequency, zonal velocity, and meridional velocity taken prior to the large vertical velocity perturbations. Mean profiles are shown in black.

3. Results

a. Observed wave properties

1) LARGE-SCALE OBSERVATIONS

Between 2 and 4 January 2011, two EM-APEX floats were advected eastward over the northern segment of the SFZ, a chain of seamounts and large bathymetric features that extends between the Antarctic Peninsula and the South American continental shelf. They maintained a horizontal separation of approximately 4 km during this period. The boxed area in Fig. 1 marks this region, and all subsequent analysis is concentrated within it. The upper-ocean buoyancy frequency and velocity upstream of the SFZ are shown in Fig. 5 as an average of 20 profiles. The mean zonal flow speed between 100 and 1500 m was 33 cm s^{-1} , with a vertical shear of $1.35 \times 10^{-4} \text{ s}^{-1}$. The mean meridional flow over the same depth range was 2 cm s^{-1} , with some variability between profiles and no significant shear. There also exists a minimum in buoyancy frequency at 350-m depth, which may reflect upward-propagating internal waves with a frequency greater than $1.4 \times 10^{-3} \text{ rad s}^{-1}$.

Figure 6a displays the measured depth-averaged horizontal flow vectors around the SFZ as well as the standard deviation of vertical water velocity measured below 100-m depth, shown by the vector shading. In the lee of a large topographic ridge, oscillatory vertical velocity perturbations with an amplitude exceeding 20 cm s^{-1} were measured by both floats, resulting in

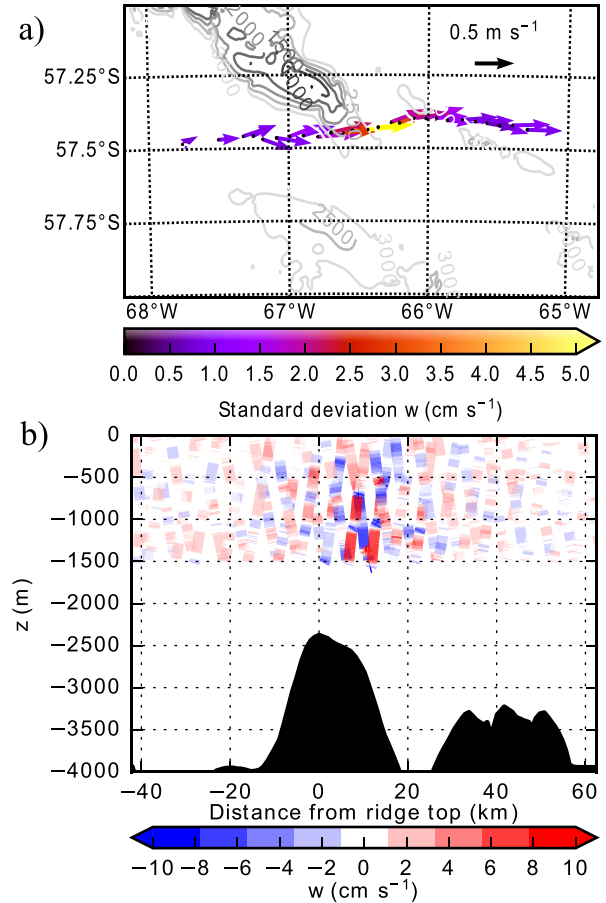


FIG. 6. (a) Mean horizontal velocity vector below 100 m within the boxed region in Fig. 1. Arrow color denotes the standard deviation of vertical velocity measured below 100-m depth. Depth is contoured in 500-m increments. (b) A vertical section of vertical velocity from the same region. The observations from both floats are superimposed, and topography from the [Smith and Sandwell \(1997\)](#) database is shaded.

large values of vertical velocity standard deviation. Away from this region, vertical velocity measurements were typically less than 2 cm s^{-1} . Figure 6b displays a section of vertical velocity as a function of height and distance from the ridge crest. The largest vertical velocities were measured within 20 km of the crest. The sawtoothlike trajectory is typical of a profiling float being advected by a strong mean flow. All the topographic data used originate from version 17.1 of the [Smith and Sandwell \(1997\)](#) global bathymetric database, since high-resolution multibeam bathymetric measurements were not available.

Figure 4 shows velocity and buoyancy perturbations from a sequence of profiles centered on the largest vertical velocity signal. Vertical velocity from these profiles were binned and displayed as a histogram in Fig. 2, from which it can be seen that the distribution of velocity

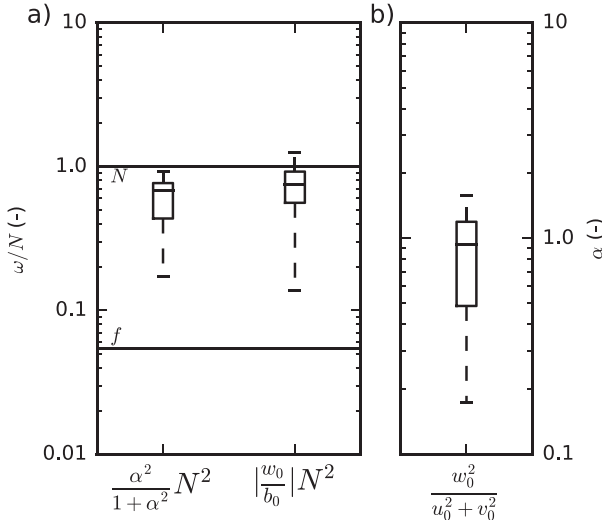


FIG. 7. (a) Two estimates of frequency normalized by the local buoyancy frequency, displayed as box and whisker plots. The estimates were obtained using Eqs. (A9) and (A10), which label the x axis. The inner line of each box denotes the median frequency. The two horizontal lines indicate the buoyancy frequency N and inertial frequency f . (b) A box and whisker plot of the aspect ratio $\alpha = k_h/m$, estimated from the velocity amplitudes.

differs greatly from the far-field mean. The greatest vertical displacement of density surfaces, estimated as b_0/N^2 , was observed to be (120 ± 20) m (profile 32, float 4976). The shaded segments indicate measurements where vertical velocity amplitude exceeds 10 cm s^{-1} and also varies coherently with at least one other component of velocity. Profiles 31 and 32 from float 4976 and profiles 26 and 27 from float 4977 contain such segments. These four profiles are used in the following analysis to quantify the wave properties. While Fig. 4 shows several other profiles that contain less conspicuous wavelike signals, noise in the horizontal velocity and buoyancy components makes it difficult to confidently assess wave properties from those profiles.

2) FREQUENCY AND ASPECT RATIO

Figure 7a amalgamates the observational estimates of aspect ratio and frequency from 14 sets of maxima from four profiles (those shaded in Fig. 4) into box and whisker diagrams. The mean aspect ratio is 1.0 ± 0.6 . Using Eq. (A9), the mean frequency is $(1.8 \pm 1) \times 10^{-3} \text{ rad s}^{-1}$, and using Eq. (A10), it is $(1.4 \pm 0.4) \times 10^{-3} \text{ rad s}^{-1}$. Both values are close to the local-mean buoyancy frequency $N \approx 2.2 \times 10^{-3} \text{ rad s}^{-1}$ and one order of magnitude larger than the local inertial frequency $f \approx 1.2 \times 10^{-4} \text{ rad s}^{-1}$. The period associated with the estimated frequency is approximately 1 h. The spread of results is a consequence of the limited profiling speed, which is likely capturing the gradually changing characteristics of a

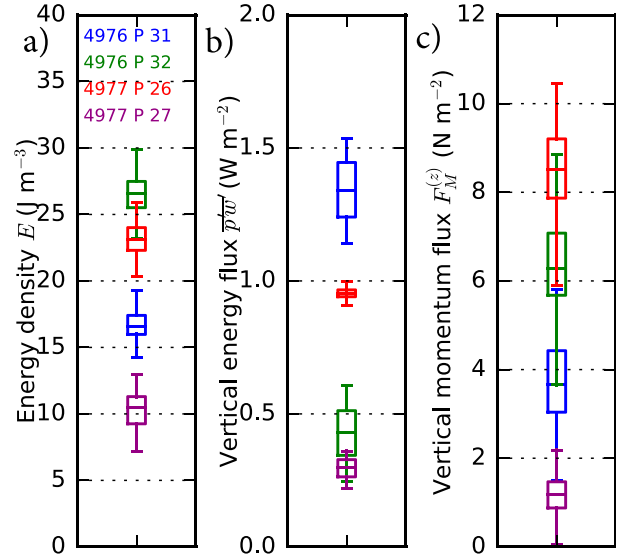


FIG. 8. Estimates of (a) energy density E , (b) vertical energy flux $\bar{w}'p'$, and (c) vertical flux of horizontal momentum $F_M^{(z)}$. The error bars are displayed as box and whisker plots derived from a bootstrapping technique. The inner box contains 50% of estimates, the central line denotes the median, and outer whiskers encompass the full range of estimates.

wave propagating through a vertical shear and non-uniform stratification.

3) ENERGY AND MOMENTUM FLUXES

The shaded regions in Fig. 4 indicate the isolated sections for which energy density and vertical fluxes of energy and horizontal momentum were calculated. The peak energy density was found to be $26 \pm 4 \text{ J m}^{-3}$ in profile 32, float 4976. Results from the four main profiles are displayed in Fig. 8a as box and whisker plots and range in magnitude from 10 to 26 J m^{-3} .

Observational estimates for the time-mean quantities $\bar{w}'p'$ and $F_M^{(z)}$, respectively representing the vertical fluxes of energy and horizontal momentum, are displayed in Figs. 8b and 8c. The peak energy flux was $1.3 \pm 0.2 \text{ W m}^{-2}$. All fluxes are positive, indicating upward wave propagation. The smallest value was found for profile 27 from float 4977, where the wave signal occurs higher in the water column, consistent with the group velocity diminishing as the depth of minimum N is approached. The average vertical group velocity corresponding to the observed flux and energy density is, following Eq. (A15), found to be $4 \pm 1 \text{ cm s}^{-1}$. These energy flux diagnostics are likely to be underestimates because of limitations in the method for estimating p' . For a wave with $\alpha \sim 1$, the hydrostatic approximation on which estimation of p' relies (Nash et al. 2005) holds only weakly. However, tests performed on a series of

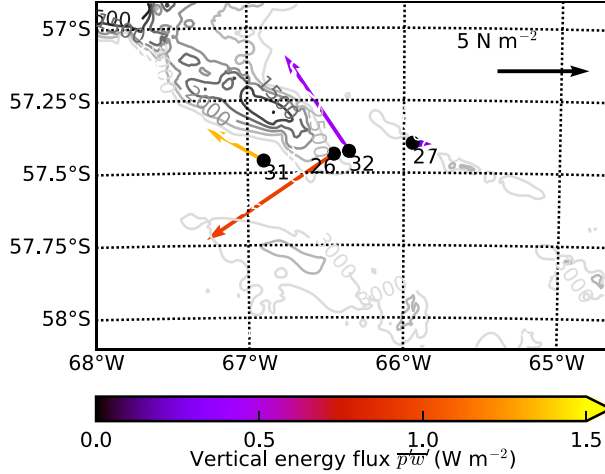


FIG. 9. Vertical flux of horizontal momentum vectors $\rho_0(\bar{w}'u', \bar{w}'v')$, labeled by profile number. Arrow color denotes the vertical energy flux. Depth is contoured in 500-m increments.

synthetic waves with α in the range 0.5 to 1.5 indicate that the method is typically in error by less than a factor of 2. So while the uncertainty on the measured energy flux is substantial, the order of magnitude is correct and the real peak value is likely to be closer to 2 W m^{-2} .

Estimates of the vertical flux of horizontal momentum range from 1 to 8 N m^{-2} in magnitude. The uncertainty on individual measurements is larger than in the energy flux case because the quantity is more sensitive to oceanographic variability in the horizontal velocity. Momentum flux vectors are displayed in Fig. 9 and are oriented predominantly in the northwest–southwest quadrant. The scatter in vector direction is likely indicative of the three-dimensional nature of the wave generation process, occurring off a complex topographic feature that does not lie perpendicular to the mean flow but could also be spatial variability. In the classic textbook lee-wave problem, the momentum flux vector would be orientated in direct opposition to the mean flow. The mean zonal momentum flux was $-3.1 \pm 0.4 \text{ N m}^{-2}$, and the mean meridional momentum flux was $0.5 \pm 0.4 \text{ N m}^{-2}$. In comparison, mean flow velocity vectors are orientated eastward (Fig. 6a) in the opposite direction to the mean momentum flux. The limitations of the floats' spatiotemporal sampling of the wave mean that we cannot definitively establish whether the wave is imparting a drag on the mean flow or radiating horizontal momentum elsewhere.

b. Wave characterization with plane wave fits

EM-APEX floats profile slowly compared to the observed wave period of 1 h, and this will have caused temporal aliasing of the measurements. The apparent

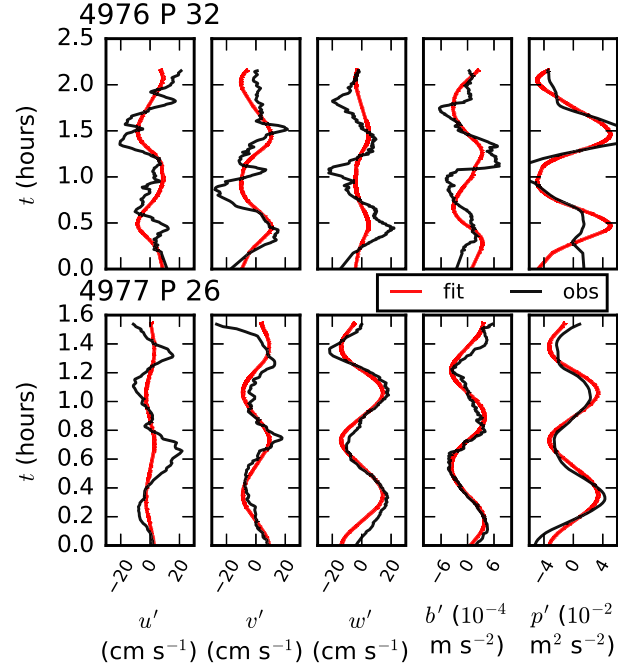


FIG. 10. Comparison of linear internal wave fits and observations for two float profiles. The quantities u' , v' , w' , b' , and p' are plotted as a function of time since start of profile.

vertical wavelength observed from subsequent maxima in vertical velocity from Fig. 4 is approximately 400 m. If the wave is stationary, its horizontal wavelength can be deduced from the Doppler relation [Eq. (A3)], as $\omega_0 = -kU$. For the observed frequency and mean flow speed, this results in an approximate zonal wavelength of 1200 m, which will be the same as the vertical wavelength for $\alpha = 1$. The conclusion from this estimate is that the intrinsic wavelength could be significantly larger than the apparent wavelength.

Fits of Eq. (A8) to measurements from two profiles chosen for having the cleanest wave signal (profile 32 from float 4976 and profile 26 from float 4977) were conducted to compare the observations to the simplest possible theoretical explanation, a monochromatic plane wave. Doing so also provides a separate determination of the vertical fluxes of energy and momentum. The resulting parameter estimates (wavenumbers and pressure perturbation) from this fitting procedure were inserted into the linear internal wave equations [Eq. (A8)] to produce the red curves in Fig. 10. The fit to profile 26 shows good agreement with observations for all variables, with the exception of u' , which is not of the correct amplitude. Profile 32 contains small-scale fluctuations in velocity that are not explained by a monochromatic plane wave; however, the large-scale variation is captured. The quantities are plotted as a function of time,

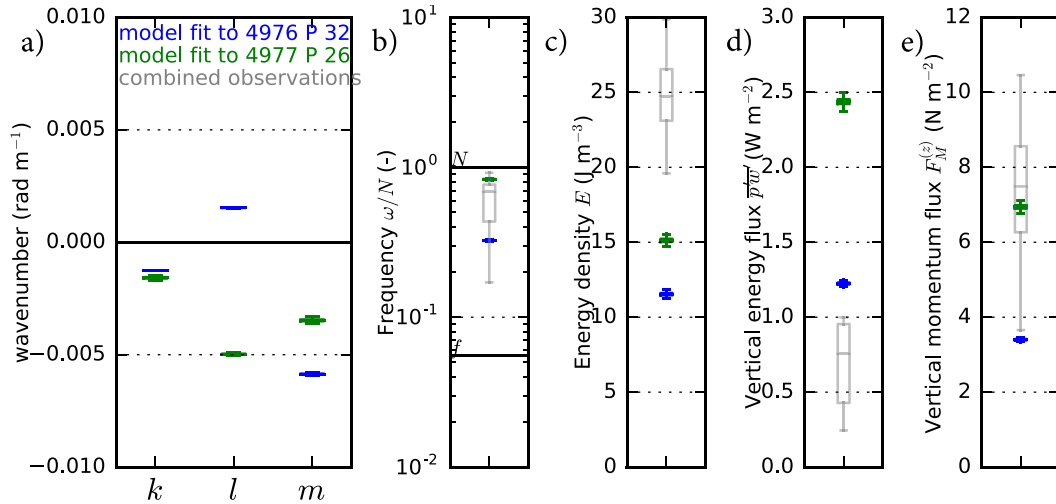


FIG. 11. Comparison of linear internal wave fit-based diagnostics and direct estimates from observations for (a) wavenumber components (for which there is no observational estimate), (b) frequency normalized by buoyancy frequency, (c) energy density, (d) vertical energy flux, and (e) vertical flux of horizontal momentum. The fits were conducted on profile 32 from float 4976 and profile 26 from float 4977.

rather than height, to remove the temporal aliasing that causes cusping, visible in Fig. 4. Cusping occurs as alternating phases of wave motion force the floats against their direction of motion, in some cases causing a complete reversal of direction, and then propel them in the same direction of motion, greatly increasing the profiling speed. Such forcing aliases the observations away from an expected sinusoidal shape.

Figure 11a shows the likelihood distributions of the plane wave–derived wavenumber components as box and whisker plots. It should be noted that the range of the distributions is typically less than 1% of the parameter value and so uncertainties are not quoted. For both profiles the fitting method finds the optimal zonal wavenumber k to be $-0.002 \text{ rad m}^{-1}$, which corresponds to a zonal wavelength of 4000 m. This is likely to be an underestimate of the real wavenumber because the fits do not reproduce the observed zonal velocity amplitude, which is related to the wavenumber by the polarization relation in Eq. (A4), and we would therefore expect a smaller zonal wavelength. There is a difference in sign between profiles as to the direction of the meridional wavenumber, likely because of the different time and position at which the profiles were taken; however, it is of similar magnitude to the zonal wavenumber. The negative sign on the zonal wavenumber is significant because it indicates that the wave phase velocity opposes the mean flow. The nonnegligible magnitude of the meridional wavenumber means that the total horizontal wave vector is not directed exactly westward against the predominantly eastward mean flow, as was also found in observational estimates of the momentum

flux vectors. The vertical wavenumber is negative, indicating upward propagation, and the vertical wavelength is 1800 m for profile 32 and 1000 m for profile 26.

The frequency determined from the fits is displayed in Fig. 11b. It overlaps with the observational estimate (gray box and whisker) and is $0.3N$ for profile 32 and $0.8N$ for profile 26. Eulerian frequencies are 3×10^{-4} and $7 \times 10^{-4} \text{ rad s}^{-1}$, corresponding to periods of 3 to 6 h. If the horizontal wavevector has been underestimated, then so have these periods following from Eqs. (A10) to (A11). Thus, the wave is not perfectly stationary, but a fixed observer would notice a significant Doppler shift.

Energy density and the vertical fluxes of energy and horizontal momentum estimates are displayed in Figs. 11c, 11d, and 11e. The energy density of the best fits are 12 and 15 J m^{-3} , smaller than the direct estimates from observations because the model has some difficulty in reproducing the full measured velocity amplitude. Energy fluxes are slightly larger than the direct estimates, at 1.2 and 2.5 W m^{-2} , but within a factor of 2. Momentum fluxes are within the bounds of the direct estimates, with values of 3.5 and 7 N m^{-2} .

In summary, while not providing a precise description, monochromatic plane waves do give a reasonable characterization of the observed lee wave. This is estimated to have horizontal and vertical wavelengths in the range of 1 to 4 km, to propagate upward and against the eastward mean flow, to be quasi stationary, and to transport energy and horizontal momentum vertically at large rates that are within a factor of 2 to 3 of the direct estimates.

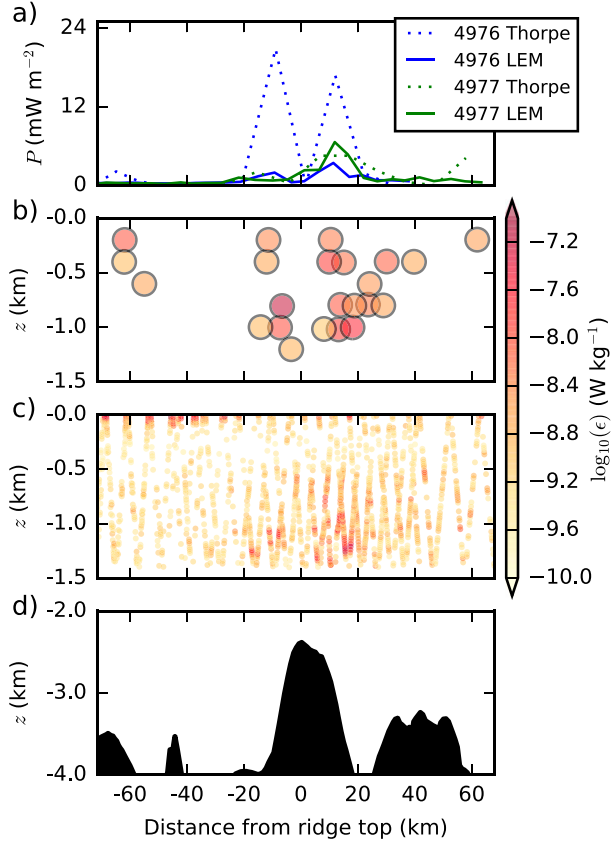


FIG. 12. (a) Depth-integrated TKED rate. (b) Thorpe-scale-derived estimate of the TKED rate on a logarithmic scale; the large circles denote 200-m bin averages. (c) LEM-derived TKED rate calculated on a 20-m sliding window. (d) Bathymetry. Measurements smaller than the noise threshold of the LEM, $c(w_{\text{noise}})^2 N$, where the noise velocity, $w_{\text{noise}} = 1 \text{ mm s}^{-1}$, has not been plotted. Similarly, portions of the water column where overturns are not detected have no associated Thorpe estimate.

c. Turbulent kinetic energy dissipation

A section of the rate of turbulent kinetic energy dissipation is displayed on a logarithmic color scale in Fig. 12. Results from Thorpe-scale analysis are shown as large circles in Fig. 12b, and results from the large-eddy method are displayed as small circles in Fig. 12c. Background levels of dissipation in Drake Passage are typically of order $10^{-10} \text{ W kg}^{-1}$, less than the detection level of either method, and are blanked out over the majority of the section. Both methods indicate a patch of high dissipation above and in the lee of the ridge crest, coincident with profiles of large vertical velocity. Notably large overturns of order 10 m in scale are detectable using the Thorpe-scale method, with dissipation rates in such patches approaching $10^{-6} \text{ W kg}^{-1}$, while the majority of overturns are smaller than this. The depth-integrated dissipation rate, $P = \int_{-Z}^0 \rho \varepsilon dz$, peaks at 20 mW m^{-2} .

Using the large-eddy method, dissipation rates are found to be largest in the profiles containing the strongest wave signal and peak at $10^{-7} \text{ W kg}^{-1}$ at roughly 1000-m depth. The depth-integrated dissipation rate peaks at 6 mW m^{-2} , significantly less than the estimated vertical flux of energy associated with the wave. The sensitivity of these results to method parameter choices was assessed by systematically varying parameters, such as filter cutoff scale and window length, over plausible ranges. The spatial distribution of dissipation did not change, but the magnitude of the integrated dissipation rate varied by up to 20%.

4. Discussion and conclusions

In this paper, observations of a wavelike feature in the vicinity of a sharp ridge made by two EM-APEX floats have been analyzed to document the feature's physical characteristics. The limited number of profiles and the necessity of considering their time-dependent nature made analysis and interpretation of some properties challenging. Nonetheless, linear internal wave theory provides a good description of the dominant mode of variability, which has a positive vertical energy flux and negative vertical wavenumber, indicating upward propagation. The zonal phase velocity is directed westward, in opposition to the mean flow, resulting in a quasi-stationary pattern, while the meridional structure of the wave appears variable. This result, deduced from coherent oscillations of velocity and buoyancy over several wave periods, leads to the conclusion that the floats observed a lee wave, likely generated at the ridge and forced by the flow of the ACC. However, naive application of infinitesimal linear wave generation theory (Bell 1975) for a near-bottom flow speed of order 20 cm s^{-1} , near-bottom stratification of $1 \times 10^{-3} \text{ rad s}^{-1}$, and topographic wavelength of 40 km implies that the resulting wave would be evanescent. This is in contradiction to the observations, which indicate a wave of frequency near N and wavelength closer to 4 km in the uppermost 1500 m of the water column.

This contradiction may be resolved by considering the steepness parameter s . The steepness parameter is defined as the ratio of topographic height h to characteristic wave height U/N , giving Nh/U for a given near-bottom flow speed and stratification (Nikurashin and Ferrari 2010). Large values of s imply that the flow does not have sufficient kinetic energy to fully mount the topography, such that a deeper portion of the water column may be blocked or diverted, making the wave generation process highly nonlinear. The value at which this transition occurs is in the range of 0.4 to 0.7, depending on topographic configuration (Aguilar and

Sutherland 2006; Nikurashin et al. 2014). Infinitesimal linear theory requires that the steepness parameter be much less than this value range. Given that the ridge height is roughly 1500 m and that near-bottom stratification, as measured from ship-based CTD casts, is $0.8 \times 10^{-3} \text{ rad s}^{-1}$, flow speeds in excess of 3 m s^{-1} would be required for a sufficiently small steepness parameter. This is not a physically reasonable speed for a near-bottom oceanic flow, and we conclude that the flow is highly likely to be blocked below some depth.

High-resolution modeling efforts in two and three dimensions using a domain analogous to the Drake Passage (Nikurashin et al. 2014) show that, for large values of the steepness parameter, the time-mean energy flux into lee waves saturates at 10 mW m^{-2} . For very long ridges in which the flow configuration is largely two-dimensional, the energy flux at generation saturates at 100 mW m^{-2} . These values are smaller than the energy fluxes estimated from our observations, of order 1 W m^{-2} , which are in good agreement with those for a propagating monochromatic plane wave constrained by linear theory. It is possible to estimate the expected energy flux from linear theory (Bell 1975) for the portion of the water column above which blocking occurs. Doing so reduces the height of the topography to an effective height h_e . Taking $h_e = 200 \text{ m}$, for which the topographic wavelength is roughly equal to the observed zonal wavelength of 4000 m, extrapolating the observed mean flow speed to be 0.2 m s^{-1} near ridge top, and using the ship-based CTD estimate of stratification, we get a linear energy flux value of 0.5 W m^{-2} . This value is within a factor 3 of the observed value. We conclude that our observations are consistent with linear generation above a blocking level. However, we also acknowledge that important small-scale bathymetric features may exist that are not resolved by the database used (Smith and Sandwell 1997).

Observed integrated dissipation rates in the Southern Ocean (St. Laurent et al. 2012; Sheen et al. 2013) are typically less than 5 mW m^{-2} . Our estimated values are similar to this; however, there is some uncertainty in this result due to quantitative limitations of the Thorpe-scale and large-eddy methods. A significant finding of our work is that the diagnosed vertical energy flux is almost two orders of magnitude larger than the depth-integrated dissipation rate. This result lends support to the idea that not all lee-wave energy is dissipated locally (Waterman et al. 2014); however, we are not able to deduce the fate of the wave energy from the limited observations available.

It is possible to make a basic assessment of the wave's propensity to shear instability using the Richardson number $Ri = N^2/(\partial u/\partial z)^2$. A necessary condition for shear instability is that $Ri < 1/4$ (Miles 1961; Howard

1961). For a single wave, the induced vertical shear $\partial u/\partial z = u_0 m$, where u_0 is the horizontal velocity amplitude and m is the vertical wavenumber. For the criterion to be satisfied, we find that $m > 0.01 \text{ rad m}^{-1}$. The observations indicate that m is less than this value by a factor of 2 to 4. In a process distinct from shear instability, a wave will become statically unstable when the ratio of the horizontal velocity amplitude to the horizontal phase speed $u_0 \omega/k > 1$ (Orlanski and Bryan 1969), and evidence from numerical models suggests that this can occur at slightly less than 1 (Liu et al. 2010). Our estimate for the static stability is in the range 0.1 to 0.25, within a factor of 4 to 10 of the condition. These estimates indicate that the wave, at its point of observation, is on the verge of undergoing shear and/or static instability. Interaction with the mean flow, changing stratification, or other waves may play a role in inducing or amplifying such instabilities.

A significant fraction of the diagnosed vertical flux of horizontal momentum associated with the wave was oriented in opposition to the mean flow, which is approximately zonal. Significant nonzonal components of the momentum flux are likely a consequence of the nonlinear, three-dimensional nature of the generation process but could also be a result of spatiotemporal variability or advection. It was not possible to deduce the divergence of the momentum flux and therefore the implied drag force. However, the magnitude of the flux is more than two orders of magnitude greater than the time-mean wind stress on the ACC (Wunsch 1998), suggesting that lee waves have the potential to be a significant term in the local momentum budget of ACC jets, as suggested by Naveira Garabato et al. (2013). Further work will be needed to understand the temporal and spatial occurrence of such wave events, and a targeted observational campaign will be required to conclusively test this hypothesis.

This paper documents the first unambiguous observation of a lee wave in the ACC. A thorough analysis of sparse observations was conducted to produce optimal estimates of wave properties, which are broadly consistent with inferences from previous, spatially incoherent finescale measurements. The extremely energetic nature of the wave is conducive to large vertical fluxes of energy and momentum and to the generation of significant amounts of turbulence, reinforcing the current appreciation for the dynamically important role that lee waves likely play in the circulation of the Southern Ocean.

Acknowledgments. The DIMES experiment was funded by the U.K. Natural Environment Research Council (NERC) Grant NE/E007058/1 (awarded to Alberto Naveira Garabato and David Smeed) and the U.S. National Science Foundation (NSF). JC acknowledges the

support of an NERC Ph.D. scholarship. ACNG acknowledges the support of a Philip Leverhulme Prize, the Royal Society, and the Wolfson Foundation. JG acknowledges the support of NSF Grants OCE-0623177 and OCE-1129564. We thank three anonymous reviewers for their insightful comments and suggestions that helped to improve the paper.

APPENDIX

Linear Internal Wave Theory

We summarize here the results of linear internal wave theory that are used in the analysis of observations, following Gill (1982). The linearized, Boussinesq momentum equations for an incompressible fluid assuming a constant stratification N , constant Coriolis parameter f , and constant mean flow $\mathbf{U} = (U, V, 0)$ can be combined into the following equation for vertical velocity perturbations w' :

$$\left[\left(\frac{\partial}{\partial t} + \mathbf{U} \cdot \nabla \right)^2 \nabla^2 + f^2 \frac{\partial^2}{\partial z^2} + N^2 \left(\frac{\partial^2}{\partial x^2} + \frac{\partial^2}{\partial y^2} \right) \right] w' = 0. \quad (\text{A1})$$

Plane wave solutions are assumed such that

$$w' = w_0 e^{i(\mathbf{k} \cdot \mathbf{x} - \omega t)}, \quad (\text{A2})$$

where w_0 is the velocity amplitude, $\mathbf{k} = (k, l, m)$ is the wavevector, $\mathbf{x} = (x, y, z)$ is the position vector, and ω is the Eulerian frequency as would be measured in a frame of reference stationary with respect to Earth. Substituting this solution into Eq. (A1) gives the familiar internal wave dispersion relation

$$(\omega - \mathbf{k} \cdot \mathbf{U})^2 = \omega_0^2 = \frac{f^2 m^2 + (k^2 + l^2)N^2}{k^2 + l^2 + m^2}, \quad (\text{A3})$$

where ω_0 is the intrinsic wave frequency. It can be seen that the intrinsic frequency of a propagating wave measured by an observer traveling with the flow must lie between f and N , else the frequency would be imaginary and the solution evanescent. In the presence of a mean flow \mathbf{U} , a Doppler-shifted (Eulerian) frequency ω would be measured by a stationary observer, and the relationship between the two frequencies is $\omega = \mathbf{k} \cdot \mathbf{U} + \omega_0$.

An internal wave generates fluctuations in all components of velocity $\mathbf{u}' = (u', v', w')$ as well as pressure p' and buoyancy b' . Here, we have divided pressure by mean density $p' = P'/\rho_0$ and define buoyancy as $b' = -gp'/\rho_0$. The relative amplitude of these

fluctuations are related to the wavelength scales by the polarization relations

$$u_0 = \frac{k\omega_0 + ilf}{\omega_0^2 - f^2} p_0, \quad (\text{A4})$$

$$v_0 = \frac{l\omega_0 - ikf}{\omega_0^2 - f^2} p_0, \quad (\text{A5})$$

$$w_0 = \frac{-m\omega_0}{N^2 - \omega_0^2} p_0, \quad \text{and} \quad (\text{A6})$$

$$b_0 = \frac{imN^2}{N^2 - \omega_0^2} p_0. \quad (\text{A7})$$

The final plane wave solutions for velocity, buoyancy, and pressure are then given by

$$(u', v', w', b', p') = (u_0, v_0, w_0, b_0, p_0) e^{i(\mathbf{k} \cdot \mathbf{x} - \omega t)}. \quad (\text{A8})$$

Thus, for a given mean flow speed, stratification, and Coriolis parameter, linear waves are completely described by a few key parameters: the components of wavenumber (inverse wavelength) in all three directions and the amplitude of the pressure perturbation. Frequency is fixed by the ratio of horizontal to vertical wavenumber or aspect ratio $\alpha^2 = (k^2 + l^2)/m^2$. The amplitude of velocity fluctuations is set by the pressure perturbation amplitude and wavenumber. Much information can therefore be deduced from limited observations of a few key variables.

By dividing the Eqs. (A6) and (A7), one gets a succinct measure of the wave frequency from the amplitude of buoyancy and vertical velocity perturbations:

$$\left| \frac{w_0}{b_0} \right| N^2 = \omega_0. \quad (\text{A9})$$

The dispersion relation can be recast in terms of the aspect ratio:

$$\omega_0^2 = \frac{f^2 + \alpha^2 N^2}{1 + \alpha^2}. \quad (\text{A10})$$

Equations (A9) and (A10) provide two methods for deducing internal wave frequency from measurements of velocity and buoyancy amplitude made by EM-APEX floats, both of which are used in subsequent analysis. For a nonhydrostatic wave, where $N \geq \omega_0 \gg f$, it can be shown using Eqs. (A4), (A5), and (A6) that the aspect ratio is related to the velocity amplitudes, as follows:

$$\frac{w_0^2}{u_0^2 + v_0^2} \approx \alpha^2, \quad (\text{A11})$$

and this result can be substituted into Eq. (A10) to deduce the intrinsic frequency from velocity amplitude alone.

a. Energy flux

Internal waves have an energy density E , consisting of a kinetic part relating to the motion of water parcels, and a potential part relating to the displacement of density surfaces from equilibrium:

$$E = \frac{1}{2}\rho_0(\overline{u'^2} + \overline{v'^2} + \overline{w'^2}) + \frac{1}{2}\rho_0N^{-2}\overline{b'^2}. \quad (\text{A12})$$

Here, an overbar denotes an average over one wave period. Linear internal waves flux energy in the direction of the group velocity \mathbf{c}_g , so that the energy flux vector is given by

$$\mathbf{F}_E = E\mathbf{c}_g, \quad (\text{A13})$$

which is also defined more generally as the average covariance of pressure and velocity perturbations:

$$\mathbf{F}_E = \rho_0\overline{p'\mathbf{u}'}. \quad (\text{A14})$$

Often one is interested in the vertical energy flux $F_E^{(z)}$, which is simply the energy density multiplied by the vertical component of the group velocity:

$$F_E^{(z)} = Ec_g^{(z)} \quad (\text{A15})$$

or, alternatively,

$$F_E^{(z)} = \rho_0\overline{p'w'}. \quad (\text{A16})$$

The equation for the vertical component of the group velocity can be derived by taking the derivative of the dispersion relation [Eq. (A10)] with respect to vertical wavenumber $\partial\omega_0/\partial m$, giving the result

$$c_g^{(z)} = \frac{-(N^2 - f^2)\alpha^2}{m(1 + \alpha^2)^{3/2}(f^2 + \alpha N^2)^{1/2}}. \quad (\text{A17})$$

It can be seen that, for fixed α , the vertical group velocity increases with wavelength (inverse wavenumber) and has opposite sign to the wavenumber, such that negative vertical wavenumber indicates upward group velocity and upward energy flux. To estimate vertical energy fluxes from observations requires knowledge of energy density, aspect ratio, and wavelength before applying these in Eqs. (A15) and (A17) (e.g., Kunze and Sanford 1984). Alternatively, it can be estimated from measurements of pressure perturbation and vertical velocity, applying Eq. (A16) (e.g., Nash et al. 2005).

b. Momentum flux

The absolute vertical flux of horizontal momentum is defined as

$$F_M^{(z)} = \rho_0[(\overline{u'w'})^2 + (\overline{v'w'})^2]^{1/2}, \quad (\text{A18})$$

where the covariance of velocities are summed in quadrature to account for transport of both zonal and meridional momentum. In the case of linear lee-wave generation by infinitesimal topography (e.g., Gill 1982), the vertical flux of horizontal momentum is equal in magnitude to the drag force exerted on the mean flow. If finite-amplitude effects are taken into account, including flow blocking and splitting, the drag becomes a nonlinear function of the steepness parameter (Welch et al. 2001).

REFERENCES

- Aguilar, D. A., and B. R. Sutherland, 2006: Internal wave generation from rough topography. *Phys. Fluids*, **18**, 066603, doi:[10.1063/1.2214538](https://doi.org/10.1063/1.2214538).
- Alford, M. H., J. M. Klymak, and G. S. Carter, 2014: Breaking internal lee waves at Kaena Ridge, Hawaii. *Geophys. Res. Lett.*, **41**, 906–912, doi:[10.1002/2013GL059070](https://doi.org/10.1002/2013GL059070).
- Batchelor, G. K., 2000: Flow at large Reynolds number: Effects of viscosity. *An Introduction to Fluid Dynamics*, Cambridge University Press, 264–377.
- Beard, N., I. Fer, P. Rhines, and C. Eriksen, 2012: Dissipation of turbulent kinetic energy inferred from Seagliders: An application to the eastern Nordic Seas overflows. *J. Phys. Oceanogr.*, **42**, 2268–2282, doi:[10.1175/JPO-D-12-094.1](https://doi.org/10.1175/JPO-D-12-094.1).
- Bell, T. H., 1975: Lee waves in stratified flows with simple harmonic time dependence. *J. Fluid Mech.*, **67**, 705–722, doi:[10.1017/S0022112075000560](https://doi.org/10.1017/S0022112075000560).
- Bray, N. A., and N. P. Fofonoff, 1981: Available potential energy for MODE eddies. *J. Phys. Oceanogr.*, **11**, 30–47, doi:[10.1175/1520-0485\(1981\)011<0030:APEFME>2.0.CO;2](https://doi.org/10.1175/1520-0485(1981)011<0030:APEFME>2.0.CO;2).
- Dillon, T. M., 1982: Vertical overturns: A comparison of Thorpe and Ozmidov length scales. *J. Geophys. Res.*, **87**, 9601–9613, doi:[10.1029/JC087iC12p09601](https://doi.org/10.1029/JC087iC12p09601).
- Ferron, B., H. Mercier, K. Speer, A. Gargett, and K. Polzin, 1998: Mixing in the Romanche Fracture Zone. *J. Phys. Oceanogr.*, **28**, 1929–1945, doi:[10.1175/1520-0485\(1998\)028<1929:MITRFZ>2.0.CO;2](https://doi.org/10.1175/1520-0485(1998)028<1929:MITRFZ>2.0.CO;2).
- Frajka-Williams, E., C. C. Eriksen, P. B. Rhines, and R. R. Harcourt, 2011: Determining vertical water velocities from Seaglider. *J. Atmos. Oceanic Technol.*, **28**, 1641–1656, doi:[10.1175/2011JTECHO830.1](https://doi.org/10.1175/2011JTECHO830.1).
- Fritts, D. C., 2003: Gravity wave dynamics and effects in the middle atmosphere. *Rev. Geophys.*, **41**, 1003, doi:[10.1029/2001RG000106](https://doi.org/10.1029/2001RG000106).
- Gargett, A., and T. Garner, 2008: Determining Thorpe scales from ship-lowered CTD density profiles. *J. Atmos. Oceanic Technol.*, **25**, 1657–1670, doi:[10.1175/2008JTECHO541.1](https://doi.org/10.1175/2008JTECHO541.1).
- Gill, A. E., 1982: *Atmosphere–Ocean Dynamics*. Academic Press, 662 pp.
- Gille, S. T., K. Speer, J. R. Ledwell, and A. C. Naveira Garabato, 2007: Mixing and stirring in the Southern Ocean. *Eos, Trans. Amer. Geophys. Union*, **88**, 382–383, doi:[10.1029/2007EO390002](https://doi.org/10.1029/2007EO390002).
- Gregg, M. C., and E. Kunze, 1991: Shear and strain in Santa Monica Basin. *J. Geophys. Res.*, **96**, 16 709–16 719, doi:[10.1029/91JC01385](https://doi.org/10.1029/91JC01385).

- Hibiya, T., N. Furuichi, and R. Robertson, 2012: Assessment of fine-scale parameterizations of turbulent dissipation rates near mixing hotspots in the deep ocean. *Geophys. Res. Lett.*, **39**, L24601, doi:[10.1029/2012GL054068](https://doi.org/10.1029/2012GL054068).
- Howard, L. N., 1961: Note on a paper of John W. Miles. *J. Fluid Mech.*, **10**, 509–512, doi:[10.1017/S0022112061000317](https://doi.org/10.1017/S0022112061000317).
- IOC, SCOR, and IAPSO, 2010: The International Thermodynamic Equation of Seawater—2010: Calculation and use of thermodynamic properties. Intergovernmental Oceanographic Commission, Manuals and Guides 56, 220 pp. [Available online at http://www.teos-10.org/pubs/TEOS-10_Manual.pdf].
- Kantha, L. H., and C. A. Clayson, 2000: *Small Scale Processes in Geophysical Fluid Flows*. International Geophysics Series, Vol. 67, Academic Press, 888 pp.
- Kilbourne, B. F., and J. B. Girton, 2015: Quantifying high-frequency wind energy flux into near-inertial motions in the southeast Pacific. *J. Phys. Oceanogr.*, **45**, 369–386, doi:[10.1175/JPO-D-14-0076.1](https://doi.org/10.1175/JPO-D-14-0076.1).
- Kunze, E., and T. B. Sanford, 1984: Observations of near-inertial waves in a front. *J. Phys. Oceanogr.*, **14**, 566–581, doi:[10.1175/1520-0485\(1984\)014<0566:OONIWI>2.0.CO;2](https://doi.org/10.1175/1520-0485(1984)014<0566:OONIWI>2.0.CO;2).
- , L. K. Rosenfeld, G. S. Carter, and M. C. Gregg, 2002: Internal waves in Monterey Submarine Canyon. *J. Phys. Oceanogr.*, **32**, 1890–1913, doi:[10.1175/1520-0485\(2002\)032<1890:IWIMSC>2.0.CO;2](https://doi.org/10.1175/1520-0485(2002)032<1890:IWIMSC>2.0.CO;2).
- , E. Firing, J. M. Hummon, T. K. Chereskin, and A. M. Thurnherr, 2006: Global abyssal mixing inferred from lowered ADCP shear and CTD strain profiles. *J. Phys. Oceanogr.*, **36**, 1553–1576, doi:[10.1175/JPO2926.1](https://doi.org/10.1175/JPO2926.1).
- Ledwell, J. R., E. Montgometry, K. L. Polzin, L. St. Laurent, R. W. Schmitt, and J. M. Toole, 2000: Evidence for enhanced mixing over rough topography in the abyssal ocean. *Nature*, **403**, 179–182, doi:[10.1038/35003164](https://doi.org/10.1038/35003164).
- Liu, W., F. P. Bretherton, Z. Liu, L. Smith, H. Lu, and C. J. Rutland, 2010: Breaking of progressive internal gravity waves: Convective instability and shear instability. *J. Phys. Oceanogr.*, **40**, 2243–2263, doi:[10.1175/2010JPO4432.1](https://doi.org/10.1175/2010JPO4432.1).
- McFarlane, N. A., 1987: The effect of orographically excited gravity wave drag on the general circulation of the lower stratosphere and troposphere. *J. Atmos. Sci.*, **44**, 1775–1800, doi:[10.1175/1520-0469\(1987\)044<1775:TEOOEG>2.0.CO;2](https://doi.org/10.1175/1520-0469(1987)044<1775:TEOOEG>2.0.CO;2).
- Merckelbach, L., D. Smeed, and G. Griffiths, 2010: Vertical water velocities from underwater gliders. *J. Atmos. Oceanic Technol.*, **27**, 547–563, doi:[10.1175/2009JTECH0710.1](https://doi.org/10.1175/2009JTECH0710.1).
- Meyer, A., K. L. Polzin, B. M. Sloyan, and H. E. Phillips, 2016: Internal waves and mixing near the Kerguelen Plateau. *J. Phys. Oceanogr.*, **46**, 417–437, doi:[10.1175/JPO-D-15-0055.1](https://doi.org/10.1175/JPO-D-15-0055.1).
- Miles, J. W., 1961: On the stability of heterogeneous shear flows. *J. Fluid Mech.*, **10**, 496–508, doi:[10.1017/S0022112061000305](https://doi.org/10.1017/S0022112061000305).
- Millard, R. C., W. B. Owens, and N. P. Fofonoff, 1990: On the calculation of the Brunt–Väisälä frequency. *Deep-Sea Res.*, **37**, 167–181, doi:[10.1016/0198-0149\(90\)90035-T](https://doi.org/10.1016/0198-0149(90)90035-T).
- Munk, W., 1980: Internal waves and small-scale processes. *Evolution of Physical Oceanography: Scientific Surveys in Honor of Henry Stommel*, B. A. Warren, and C. Wunsch, Eds., MIT Press, 264–290.
- Nash, J. D., M. H. Alford, and E. Kunze, 2005: Estimating internal wave energy fluxes in the ocean. *J. Atmos. Oceanic Technol.*, **22**, 1551–1570, doi:[10.1175/JTECH1784.1](https://doi.org/10.1175/JTECH1784.1).
- Naveira Garabato, A. C., K. L. Polzin, B. A. King, K. J. Heywood, and M. Visbeck, 2004: Widespread intense turbulent mixing in the Southern Ocean. *Science*, **303**, 210–213, doi:[10.1126/science.1090929](https://doi.org/10.1126/science.1090929).
- , J. G. Nurser, R. B. Scott, and J. A. Goff, 2013: The impact of small-scale topography on the dynamical balance of the ocean. *J. Phys. Oceanogr.*, **43**, 647–668, doi:[10.1175/JPO-D-12-056.1](https://doi.org/10.1175/JPO-D-12-056.1).
- Nikurashin, M., and R. Ferrari, 2010: Radiation and dissipation of internal waves generated by geostrophic motions impinging on small-scale topography: Application to the Southern Ocean. *J. Phys. Oceanogr.*, **40**, 2025–2042, doi:[10.1175/2010JPO4315.1](https://doi.org/10.1175/2010JPO4315.1).
- , and —, 2011: Global energy conversion rate from geostrophic flows into internal lee waves in the deep ocean. *Geophys. Res. Lett.*, **38**, L08610, doi:[10.1029/2011GL046576](https://doi.org/10.1029/2011GL046576).
- , —, N. Grisvard, and K. Polzin, 2014: The impact of finite-amplitude bottom topography on internal wave generation in the Southern Ocean. *J. Phys. Oceanogr.*, **44**, 2938–2950, doi:[10.1175/JPO-D-13-0201.1](https://doi.org/10.1175/JPO-D-13-0201.1).
- Orlanski, I., and K. Bryan, 1969: Formation of the thermocline step structure by large-amplitude internal gravity waves. *J. Geophys. Res.*, **74**, 6975–6983, doi:[10.1029/JC074i028p06975](https://doi.org/10.1029/JC074i028p06975).
- Peters, H., M. C. Gregg, and T. B. Sanford, 1995: Detail and scaling of turbulent overturns in the Pacific Equatorial Undercurrent. *J. Geophys. Res.*, **100**, 18 349–18 368, doi:[10.1029/95JC01360](https://doi.org/10.1029/95JC01360).
- Phillips, H. E., and N. L. Bindoff, 2014: On the nonequivalent barotropic structure of the Antarctic Circumpolar Current: An observational perspective. *J. Geophys. Res. Oceans*, **119**, 5221–5243, doi:[10.1002/2013JC009516](https://doi.org/10.1002/2013JC009516).
- Pinkel, R., M. Buijsman, and J. Klymak, 2012: Breaking topographic lee waves in a tidal channel in Luzon Strait. *Oceanography*, **25**, 160–165, doi:[10.5670/oceanog.2012.51](https://doi.org/10.5670/oceanog.2012.51).
- Polzin, K. L., A. C. Naveira Garabato, T. N. Huussen, B. M. Sloyan, and S. Waterman, 2014: Finescale parameterizations of turbulent dissipation. *J. Geophys. Res. Oceans*, **119**, 1383–1419, doi:[10.1002/2013JC008979](https://doi.org/10.1002/2013JC008979).
- Sanford, T. B., 1971: Motionally induced electric and magnetic fields in the sea. *J. Geophys. Res.*, **76**, 3476–3492, doi:[10.1029/JC076i015p03476](https://doi.org/10.1029/JC076i015p03476).
- , J. Dunlap, J. Carlson, D. Webb, and J. B. Girton, 2005: Autonomous velocity and density profiler: EM-APEX. *Proc. IEEE/OES Eighth Working Conf. on Current Measurement Technology*, Southampton, United Kingdom, IEEE, 152–156.
- Scott, R. B., J. A. Goff, A. C. Naveira Garabato, and A. J. G. Nurser, 2011: Global rate and spectral characteristics of internal gravity wave generation by geostrophic flow over topography. *J. Geophys. Res.*, **116**, C09029, doi:[10.1029/2011JC007005](https://doi.org/10.1029/2011JC007005).
- Sheen, K., and Coauthors, 2013: Rates and mechanisms of turbulent dissipation and mixing in the Southern Ocean: Results from the Diapycnal and Isopycnal Mixing Experiment in the Southern Ocean (DIMES). *J. Geophys. Res. Oceans*, **118**, 2774–2792, doi:[10.1002/jgrc.20217](https://doi.org/10.1002/jgrc.20217).
- Smith, W. H., and D. T. Sandwell, 1997: Global sea floor topography from satellite altimetry and ship depth soundings. *Science*, **277**, 1956–1962, doi:[10.1126/science.277.5334.1956](https://doi.org/10.1126/science.277.5334.1956).
- St. Laurent, L., A. C. Naveira Garabato, J. R. Ledwell, M. Thurnherr, J. M. Toole, and J. Watson, 2012: Turbulence and diapycnal mixing in Drake Passage. *J. Phys. Oceanogr.*, **42**, 2143–2152, doi:[10.1175/JPO-D-12-027.1](https://doi.org/10.1175/JPO-D-12-027.1).
- Talley, L., 2013: Closure of the global overturning circulation through the Indian, Pacific, and Southern Oceans: Schematics and transports. *Oceanography*, **26**, 80–97, doi:[10.5670/oceanog.2013.07](https://doi.org/10.5670/oceanog.2013.07).
- Taylor, G. I., 1935: Statistical theory of turbulence. *Proc. Roy. Soc. Math. Phys. Eng. Sci.*, **151**, 421–444, doi:[10.1098/rspa.1935.0158](https://doi.org/10.1098/rspa.1935.0158).

- Thorpe, S. A., 1977: Turbulence and mixing in a Scottish loch. *Philos. Trans. Roy. Soc. London, A***286**, 125–181, doi:[10.1098/rsta.1977.0112](https://doi.org/10.1098/rsta.1977.0112).
- Thurnherr, A. M., E. Kunze, J. M. Toole, L. St. Laurent, K. J. Richards, and A. Ruiz-Angulo, 2015: Vertical kinetic energy and turbulent dissipation in the ocean. *Geophys. Res. Lett.*, **42**, 7639–7647, doi:[10.1002/2015GL065043](https://doi.org/10.1002/2015GL065043).
- Vallis, G. K., 2006: *Atmospheric and Oceanic Fluid Dynamics*. Cambridge University Press, 745 pp.
- Waterhouse, A. F., and Coauthors, 2014: Global patterns of diapycnal mixing from measurements of the turbulent dissipation rate. *J. Phys. Oceanogr.*, **44**, 1854–1872, doi:[10.1175/JPO-D-13-0104.1](https://doi.org/10.1175/JPO-D-13-0104.1).
- Waterman, S., A. C. Naveira Garabato, and K. L. Polzin, 2013: Internal waves and turbulence in the Antarctic Circumpolar Current. *J. Phys. Oceanogr.*, **43**, 259–282, doi:[10.1175/JPO-D-11-0194.1](https://doi.org/10.1175/JPO-D-11-0194.1).
- , K. L. Polzin, A. C. Naveira Garabato, K. L. Sheen, and A. Forryan, 2014: Suppression of internal wave breaking in the Antarctic Circumpolar Current near topography. *J. Phys. Oceanogr.*, **44**, 1466–1492, doi:[10.1175/JPO-D-12-0154.1](https://doi.org/10.1175/JPO-D-12-0154.1).
- Watson, A. J., J. R. Ledwell, M.-J. Messias, B. A. King, N. Mackay, M. P. Meredith, B. Mills, and A. C. Naveira Garabato, 2013: Rapid cross-density ocean mixing at mid-depths in the Drake Passage measured by tracer release. *Nature*, **501**, 408–411, doi:[10.1038/nature12432](https://doi.org/10.1038/nature12432).
- Welch, W. T., P. Smolarkiewicz, R. Rotunno, and B. A. Boville, 2001: The large-scale effects of flow over periodic mesoscale topography. *J. Atmos. Sci.*, **58**, 1477–1492, doi:[10.1175/1520-0469\(2001\)058<1477:TLSEOF>2.0.CO;2](https://doi.org/10.1175/1520-0469(2001)058<1477:TLSEOF>2.0.CO;2).
- Wunsch, C., 1998: The work done by the wind on the oceanic general circulation. *J. Phys. Oceanogr.*, **28**, 2332–2340, doi:[10.1175/1520-0485\(1998\)028<2332:TWDBTW>2.0.CO;2](https://doi.org/10.1175/1520-0485(1998)028<2332:TWDBTW>2.0.CO;2).